Front. Environ. Sci. Eng. 2021, 15(4): 52
https://doi.org/10.1007/s11783-020-1344-8

RESEARCH ARTICLE

Fabrication of highly efficient Bi_2WO_6/CuS composite for visible-light photocatalytic removal of organic pollutants and Cr(VI) from wastewater

Wei Mao[1,2], Lixun Zhang[1,2], Tianye Wang[3,4], Yichen Bai[3,4], Yuntao Guan (✉)[1,2]

1 Guangdong Provincial Engineering Technology Research Center for Urban Water Cycle and Water Environment Safety, Tsinghua Shenzhen International Graduate School, Tsinghua University, Shenzhen 518055, China
2 State Environmental Protection Key Laboratory of Microorganism Application and Risk Control, School of Environment, Tsinghua University, Beijing 100084, China
3 College of Resources and Environment, Jilin Agricultural University, Changchun 130000, China
4 Key Laboratory of Soil Resource Sustainable Utilization for Jilin Province Commodity Grain Bases, Changchun 130118, China

HIGHLIGHTS

- A novel Bi_2WO_6/CuS composite was fabricated by a facile solvothermal method.
- This composite efficiently removed organic pollutants and Cr(VI) by photocatalysis.
- The DOM could promoted synchronous removal of organic pollutants and Cr(VI).
- This composite could be applied at a wide pH range in photocatalytic reactions.
- Possible photocatalytic mechanisms of organic pollutants and Cr(VI) were proposed.

ARTICLE INFO

Article history:
Received 7 March 2020
Revised 13 August 2020
Accepted 17 August 2020
Available online 8 October 2020

Keywords:
Photocatalysis
Bi_2WO_6/CuS
Organic pollutants
Cr(VI)
Synergistic effect

GRAPHIC ABSTRACT

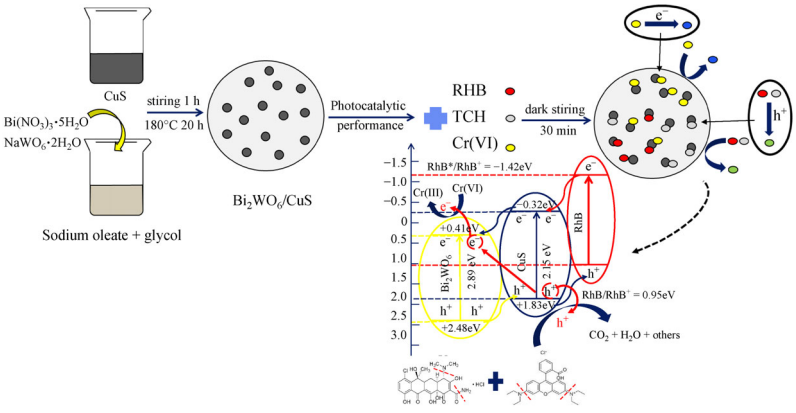

ABSTRACT

A visible-light-driven Bi_2WO_6/CuS p-n heterojunction was fabricated using an easy solvothermal method. The Bi_2WO_6/CuS exhibited high photocatalytic activity in a mixed system containing rhodamine B (RhB), tetracycline hydrochloride (TCH), and Cr (VI) under natural conditions. Approximately 98.8% of the RhB (10 mg/L), 87.6% of the TCH (10 mg/L) and 95.1% of the Cr(VI) (15 mg/L) were simultaneously removed from a mixed solution within 105 min. The removal efficiencies of TCH and Cr(VI) increased by 12.9% and 20.4%, respectively, in the mixed solution, compared with the single solutions. This is mainly ascribed to the simultaneous consumption electrons and holes, which increases the amount of excited electrons/holes and enhances the separation efficiency of photogenerated electrons and holes. Bi_2WO_6/CuS can be applied over a wide pH range (2–6) with strong photocatalytic activity for RhB, TCH and Cr(VI). Coexisiting dissolved organic matter in the solution significantly promoted the removal of TCH (from 74.7% to 87.2%) and Cr(VI) (from 75.7% to 99.9%) because it accelerated the separation of electrons and holes by consuming holes as an electron acceptor. Removal mechanisms of RhB, TCH, and Cr(VI) were proposed, Bi_2WO_6/CuS was formed into a p-n heterojunction to efficiently separate and transfer photoelectrons and holes so as to drive photocatalytic reactions. Specifically, when reducing pollutants (e.g., TCH) and oxidizing pollutants (e.g., Cr(VI)) coexist in wastewater, the p-n heterojunction in Bi_2WO_6/CuS acts as a "bridge" to shorten the electron transport and thus simultaneously increase the removal efficiencies of both types of pollutants.

✉ Corresponding author
E-mail: guanyt@tsinghua.edu.cn

1 Introduction

Organic pollutants and heavy metals co-exist in high concentrations in industrial wastewater because it is a mixture of different industrial effluents from pharmaceuticals, dyes, metal smelting, fertilizers, battery manufacturing, and electroplating (Wang et al., 2018; Ali et al., 2019). These organic and inorganic contaminants are frequently highly toxic and carcinogenic. Nevertheless, few composite materials have been designed to simultaneously and efficiently remove of organic and inorganic pollutants. Photocatalytic technology holds great promise for treating such waste streams because it is renewable, nontoxic, low in cost, environmentally sustainable, and requires simple reaction conditions (Padervand and Jalilian, 2019). Stable catalysts that respond strongly to visible light should be selected for photocatalytic reactions (Bai et al., 2019). Many photocatalytic materials, such as TiO_2 (Sharma et al., 2019), CuO (Ahmadi et al., 2017), and Bi_2WO_6 (Mao et al., 2018), have been used for environmental applications such as photocatalytic degradation of organic pollutants, sterilization and disinfection, photocatalytic nitrogen fixation, photocatalytic organic synthesis for carbon dioxide absorption and reduction of high-priced heavy metal ions (Wang et al., 2019a).

Bismuth tungstate (Bi_2WO_6) has recently attracted the attention of researchers trying to degrade pollutants in weastwater because of its excellent photocatalytic reactivity and stable structure (Li et al., 2018b). Pure Bi_2WO_6 nanosheets have weak visible-light response and recombine readily with photogenerated carriers. This is mainly because of the narrow range of wavelengths absorbed by pure Bi_2WO_6 from UV to visible light below 450 nm (Huang et al., 2018), which greatly restricts its application in the photocatalytic degradation of contaminants. Compared with single-component photocatalysts, composite photocatalysts usually utilize solar energy deep into the visible light range to degrade pollutants more efficiently.

Copper sulfides (CuS), is a p-type semiconductor with a narrow band gap of 2.0 eV, and has been studied because of its valence state, strong absorption of visible light, and crystal morphologies. However, pure CuS has low photocatalytic activity because of the rapid recombination of photo-induced carriers (Gao et al., 2017). Recently, various Bi_2WO_6-based composites such as $Bi_2WO_6/BiPO_4$ (Zhu et al., 2017) and Bi_2WO_6/g-C_3N_4 (Mao et al., 2018), have been fabricated as photocatalysts. Guo et al. (Guo et al., 2019) used hydrothermal reaction to prepare Bi_2WO_6/CuS, but the composite materials had a low removal efficiency for organic pollutants. In this study, Bi_2WO_6/CuS composites were synthesized by a constructing sodium oleate/glycol system in one step, which enhanced the photocatalytic performance of the Bi_2WO_6/CuS composites. The Bi_2WO_6/CuS successfully catalyzed the simultaneous oxidation of rhodamine B (RhB) and tetracycline hydrochloride (TCH) and reduction of Cr(VI) in a mixed solution, which shows its promise for the photocatalytic treatment of wastewater containing organic pollutants and heavy metal ions. The simplicity and high yield of the synthesis make the composite an attractive proposition for mass production.

The objectives of this study were as follows: 1) to fabricate Bi_2WO_6/CuS composites and analyze their physicochemical properties; 2) to investigate the photocatalytic performance of Bi_2WO_6/CuS for the removal of RhB, TCH, and Cr(VI) from single and mixed solutions under visible-light irradiation; 3) to evaluate the influence of Bi_2WO_6/CuS-3 dosage, initial pH and dissolved organic matter (DOM) on the removal of RhB, TCH, and Cr(VI) from a mixed solution; 4) to confirm the reusability and stability of the resulting photocatalyst by recycling it for four use cycles; and 5) to elucidate the primary removal mechanisms of RhB, TCH, and Cr(VI) by Bi_2WO_6/CuS in the photocatalytic reaction.

2 Experimental

2.1 Materials and reagents

Bismuth nitrate hydrate ($Bi(NO_3)_3{\cdot}5H_2O$) (99%) was obtained from Guangdong Xilong Chemical Co., Ltd. (China). Sulfourea (99%), RhB (AR, analytical grade), and potassium dichromate ($K_2Cr_2O_7$) (99%) were purchased from Aladdin, Inc. (Shanghai, China). Sodium tungstate dehydrate ($NaWO_6 \cdot 2H_2O$) (AR, analytical grade) was purchased from Shanghai Chemical Company (China). Sodium oleate (97%), copper acetate (95%), ethanediol (AR, analytical grade), and ethyl alcohol (AR, analytical grade) were acquired Sinopharm Chemical Reagent Co., Ltd. (Shanghai, China). TCH (95%) was obtained from Ai LAn Chemical Technology Co., Ltd. (Shanghai, China).

2.2 Preparation of photocatalyst

For fabricating the pristine CuS nanoparticles, 2 mmol of cupric acetate dihydrate and 2 mmol of thiourea were dissolved together in 40 mL of deionized water, stirred vigorously for 30 min. The mixture was then transferred to a 100 mL Teflonlined autoclave, and hermetically heated at 180°C for 24 h. After the system cooled naturally to room temperature, the solid precipitate generated from the reaction was collected by filtration and washed several times with ethanol and deionized water. The solid CuS was then dried for 10 h in an oven at 80°C, crushed, and stored for further use.

Sodium oleate (4 mmol) and $Bi(NO_3)_3 \cdot 5H_2O$ (4 mmol) were dissolved in 40 mL ethylene glycol orderly. Separately, $Na_2WO_4 \cdot 2H_2O$ (2 mmol) was dissolved in 20 mL ethylene glycol with heat. The two solutions were

then mixed and stirred vigorously for 1 h. A small quantity of CuS dissolved in 10 mL ethylene glycol was added to the solution, followed by ultrasonic dispersion. After stirring for 2 h, the mixture was transferred to a 100 mL Teflonlined autoclave, hermetically heated at 180°C for 20 h, and cooled to room temperature. The precipitate, i.e., Bi_2WO_6/CuS was collected by filtration, washed several times with ethanol and deionized water, and dried to constant weight in the oven at 80°C. Finally, the Bi_2WO_6/CuS was ground and stored for further use. Different Bi_2WO_6/CuS composites were synthesized by controlling the ratios of Bi_2WO_6 to CuS. Composites with Bi_2WO_6:CuS ratios of 1:1, 2:1, 4:1, and 10:1 were named Bi_2WO_6/CuS-1, Bi_2WO_6/CuS-2, Bi_2WO_6/CuS-3, and Bi_2WO_6/CuS-4, respectively.

2.3 Characterization of photocatalysts

Powder X-ray diffractometry (XRD) of solid samples was recorded by a D/MAX 2500 X-ray diffractometer (Rigaku, Japan) with a monochromatic Cu Kα radiation source, at 40 kV and 100 mA (λ = 0.15418 Å). Fourier transform infrared spectra (FT-IR) of solid samples were obtained with a Nicolet 500 FT-IR analyzer (Thermo Scientific, USA) using KBr pellets in the spectral range of 4000–400 cm^{-1}. The sizes, morphologies, and crystal lattices of solid samples were identified by scanning electron microscopy with energy dispersion spectrometry (SEM-EDS, SU8010, Hitachi, Japan) and transmission electron microscopy (TEM, FEI Tecnai G^2 F20, USA). The energy-dispersive X-ray spectra (EDS) (EDS, FEI Tecnai G^2 F20, USA) of solid samples were also measured during the TEM measurement. The surface chemical state of the Bi_2WO_6/CuS was analyzed using X-ray photoelectron spectroscopy (XPS, ULVAC-PHI, Japan). Photoluminescence (PL) spectra were measured with a fluoresce nce spectrophotometer (λEx = 338 nm, a Hitachi F-4600, Japan) at room temperature. The UV-vis diffuse reflectance spectra (UV-DRS) of solid samples were recorded by a UV-visible spectrophotometer (TU-1901, Shenzhen Yixin Instrument Equipment Limited, China) using $BaSO_4$ as a reference. Electrochemical impedance spectroscopy (EIS) and Mott-Schottky measurements (M-S) were carried out on an electro-chemical workstation (CHI-600E, Germany). Generally, the Bi_2WO_6/CuS (0.05 g) was dispersed in ethanol (5 mL) by ultrasound (F-008S, Shenzhen Fuyang Technology Limited, China) and the suspension was drop-cast onto an indium tin oxide (ITO)-coated glass (effective area approximately 12 cm^2, China) which was used as the working electrode. A calomel electrode and a platinum wire (232-01, China) were used as the reference electrode and the counter electrode, respectively, in the measurement of EIS and M-S. The EIS measurements were carried out in a 0.5 mol/L Na_2SO_4 solution at the open circuit potential in the frequency range of 10^5–10^{-2} Hz.

2.4 Photocatalytic experiments

2.4.1 Single solution

Photocatalytic experiments were first conducted using Bi_2WO_6/CuS under visible-light irradiation to treat separate solutions of RhB, TCH and Cr(VI). First, 100 mg of Bi_2WO_6/CuS was placed in a 250 mL quartz photo reactor with 100 mL aqueous solution of RhB (2–50 mg/L), TCH (2–50 mg/L), or Cr(VI) (5–35 mg/L). Before irradiation, the mixture was stirred vigorously for 30 min in the dark to attain adsorption equilibrium. The mixture was then irradiated for 105 min using a 500 W Xe lamp. Afterwards, 4 mL samples were taken and centrifuged to remove catalyst particles. The concentration of Cr(VI) was determined by the 1,5-diphenylcarbazide colorimetric method at 540 nm using a UV-visible spectrophotometer. The photocatalytic oxidation of RhB (553 nm) and TCH (375 nm) was measured under the same conditions.

2.4.2 Mixed solution

In the mixed solution experiments, 100 mg of Bi_2WO_6/CuS-3 was added to 100 mL of a mixed solution of RhB (10 mg/L), TCH (10 mg/L) and Cr(VI) (0–35 mg/L). We studied the effects of Bi_2WO_6/CuS-3 dosage, initial pH value, which was regulated using sodium hydroxide and hydrochloric acid, and DOM (glucose solution) on the simultaneous removal of RhB, TCH and Cr(VI) from the mixed solution. A UV-visible spectrophotometer was used to measure the concentrations of RhB and TCH at 553 nm and 357 nm, respectively, and the Cr(VI) concentration was measured at 540 nm via the 1,5-diphenylcarbazide colorimetric method.

2.5 Data analysis

Kinetic studies are important for understanding the mechanism of contaminant removal. The Langmuir-Hinshelwood (L-H) pseudo-first-order kinetic model was used to describe the photocatalytic removal efficiency of RhB, TCH, and Cr(VI):

$$R = K'\theta = -\frac{d_C}{d_T} = K'\left(\frac{KC}{1+KC}\right), \tag{1}$$

where R is the oxidation rate (mg/L/min), K' is the oxidation rate constant (L/min), C is the contaminant concentration (mg/L), K' is the adsorption coefficient and θ is the site coverage of the reactant. For low concentration solutions, the L-H model can be simplified to pseudo-first-order (PFO) kinetics (Eqs. (2) and (3)):

$$-\frac{d_C}{d} = -K_1 C, \tag{2}$$

$$\mathrm{Ln}\left(\frac{C}{C_0}\right) = -K_1 t, \tag{3}$$

where K_1 is the pseudo-first-order rate constant, t is the reaction time (min), and C and C_0 are the current and initial concentrations of the contaminant, respectively.

3 Results and discussion

3.1 Characterization of Bi_2WO_6/CuS

The crystal phases of Bi_2WO_6/CuS were characterized by XRD, and the results are shown in Fig. 1(a). The diffraction peaks of Bi_2WO_6/CuS heterojunctions were identified as standard phase-pure orthorhombic Bi_2WO_6 (a = 5.457 Å, b = 16.435 Å, c = 5.438 Å), according to JCPDS No. 39-0256 (Zhou et al., 2019). This result indicates that Bi_2WO_6 was successfully synthesized through solvothermal reactions. The CuS also had a phase-pure orthorhombic structure without impurities matching with JCPDS 06-0464 (Fang et al., 2018). Additionally, the XRD pattern of Bi_2WO_6/CuS matched well with that of pristine Bi_2WO_6, and no other crystalline phase was observed, suggesting that the introduction of CuS in Bi_2WO_6/CuS composite did not change the crystal lattice structure of Bi_2WO_6. The characteristic peaks of CuS were almost absent, which may be due to reduced exposure of the crystal face because of coverage by Bi_2WO_6. The peak intensity of Bi_2WO_6/CuS was higher than of Bi_2WO_6, indicating that the introduction of CuS improved the crystallization. Thus, XRD provided clear evidence that the Bi_2WO_6/CuS structures were not altered by the solvothermal reaction.

The surface functional groups, molecular structures, and the valence bond interactions of Bi_2WO_6/CuS were investigated by FT-IR. The two characteristic FT-IR peaks of Bi_2WO_6 were located at 433 cm^{-1} and 790 cm^{-1}, respectively (Fig. 1(b)). The strong peak at 790 cm^{-1} was ascribed to the antisymmetric and symmetric stretching modes of terminal O–W–O (Zargazi and Entezari, 2019). The 433 cm^{-1} peak of Bi_2WO_6 was attributed to antisymmetric modes of WO_6 octahedra. The peaks at 523 cm^{-1} and 1385 cm^{-1} corresponded to the stretching vibration peaks of Bi–O and W–O–W, respectively, which suggests the existence of Bi_2WO_6. The strong peaks at 615 cm^{-1} and 1385 cm^{-1} were the vibrational peaks of the Cu–S and Cu–O stretching modes (Li et al., 2017), and illustrate that Bi_2WO_6/CuS is uniformly mixed and connected by Cu–O bridges between Bi_2WO_6 and CuS. The spectra also showed some hydroxyl functionalities at 1430 cm^{-1}, 1640 cm^{-1}, 1643 cm^{-1}, 2852 cm^{-1}, and 3720 cm^{-1}, which were attributed to symmetric and asymmetric vibrations of aliphatic C–O–C, C = O, –OH, C–H, –OH, respectively (Loy et al., 2019). These organic functional groups may have come from sodium oleate and ethylene glycol in the reaction system. Moreover, sodium oleate provides oxygen-containing functional groups during the solvothermal reaction, which induces Bi_2WO_6/CuS to form more stable metal oxidation bonds of Bi–O and W–O and shape the photocatalytic heterojunction. Furthermore, after loading CuS, the FT-IR spectra of Bi_2WO_6/CuS-3 was significantly blue shifted, and the band intensity decreased because Bi in Bi–O bonds was replaced by Cu.

The morphological features of Bi_2WO_6/CuS-3 were studied using SEM, TEM, HRTEM, and EDS (Fig. 2). Compared with the microsphere structure of pure Bi_2WO_6 and CuS (Figs. 2(a) and 2(b)), a flower-like hierarchical structure was seen in the SEM images of Bi_2WO_6/CuS-3 (Fig. 2(c)). The structure has a high specific surface area that provides more active sites and promotes the migration of photogenerated electron-holes, thus enhancing the removal efficiency. The TEM images in Fig. 2(d) clearly show the ellipsoidal morphology of the Bi_2WO_6/CuS-3 nanoparticles, and the corresponding selected area electron diffraction (SAED) pattern revealed that the nanoparticles were polycrystalline. The interplanar spacings of Bi_2WO_6/

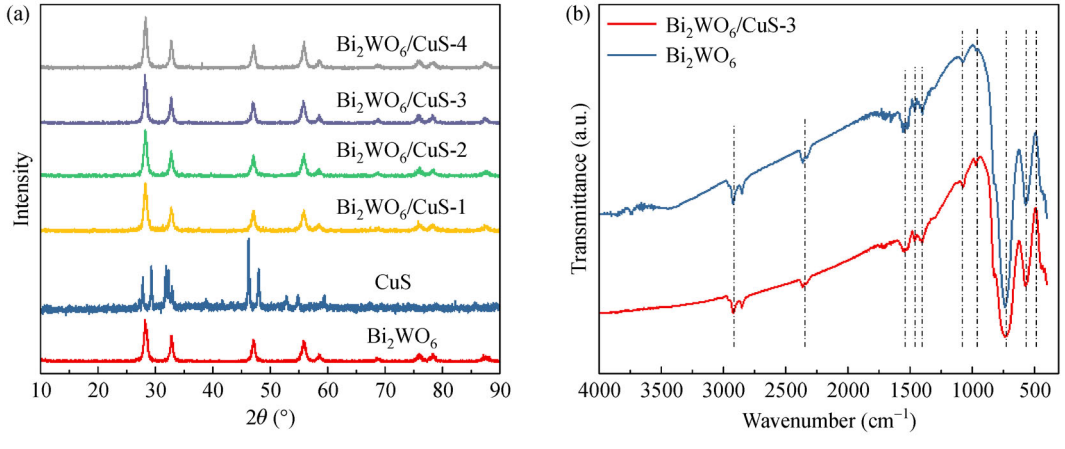

Fig. 1 (a) XRD patterns and (b) FT-IR spectra of photocatalysts.

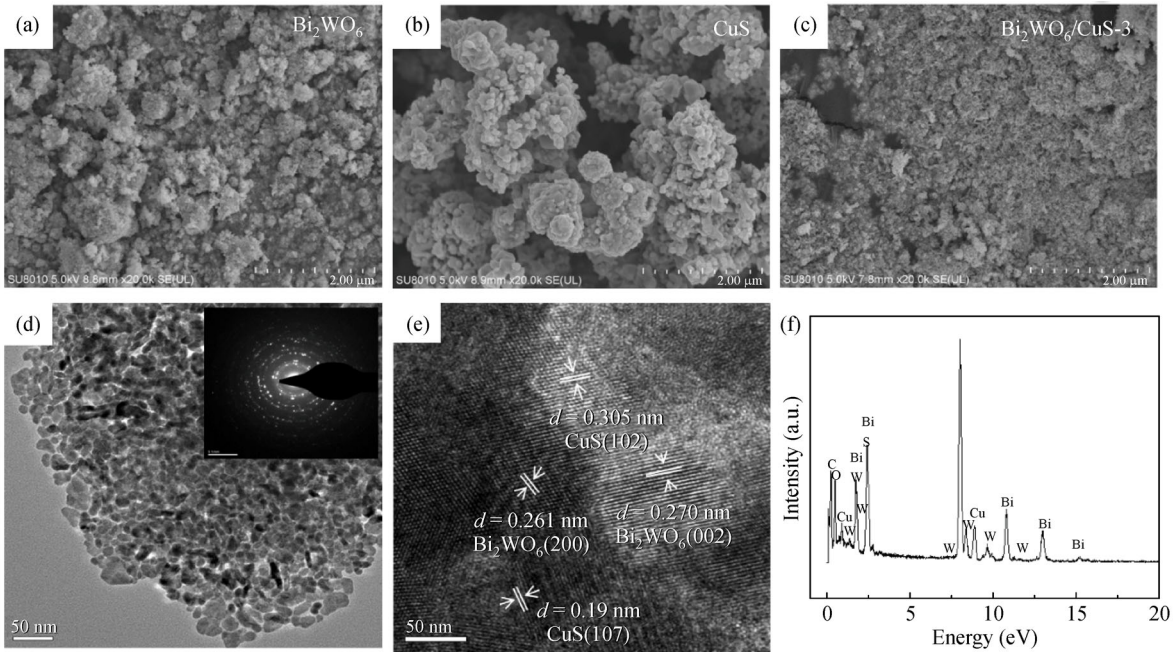

Fig. 2 SEM images of (a) Bi_2WO_6, (b) CuS, and (c) Bi_2WO_6/CuS-3; (d) –(e) TEM (SAED) and HRTEM images of Bi_2WO_6/CuS-3, and (f) EDS spectra of Bi_2WO_6/CuS-3.

CuS-3 were measured to be 0.261, 0.270, 0.19 and 0.305 nm (Fig. 2(e)), corresponding to the d-spacing for the (200) and (002) planes of Bi_2WO_6 and the (107) and (102) planes of hexagonal CuS, respectively (JCPDS No. 78-0877). Collectively, these observation agreed well with the XRD results. The major elements detected by EDS elemental microanalysis were Bi, W, S, C, O and Cu (Fig. 2(f)). This suggests that CuS was loaded onto Bi_2WO_6 by the solvothermal reaction and forms a favorable crystalline shape.

The XPS spectra were examined to determine the elemental composition and characteristic chemical state of Bi_2WO_6/CuS-3. The survey scanning spectra (Fig. 3(a)) showed the presence of W, Bi, S, Cu, C, and O in Bi_2WO_6/CuS-3. The existence of the carbon peak can be attributed to undefined carbon species in the XPS test. The high-resolution W $4f_{5/2}$ and W $4f_{7/2}$ lines were assigned to the peaks at ~34.89 eV and ~36.9 eV (Fig. 3(b)), respectively. The peaks at 158.75 eV and 164.1 eV (Fig. 3(c)) corresponded to Bi $4f_{7/2}$ and Bi $4f_{5/2}$, respectively, thereby illustrating that Bi^{3+} was the main chemical state in Bi_2WO_6/CuS-3 (Chen et al., 2018). Moreover, the high-resolution C 1s spectrum exhibited a main peak centered at ~284.6 eV (Fig. S1(a)), which may have been caused by sodium oleate and ethylene glycol in the reaction system. As shown in Fig. S1(b), O1s had a binding energy peak at ~530.7 eV. The XPS spectrum of Cu 2p had a peak at 933.41 eV that was assigned to Cu $2p_{3/2}$, indicating that Cu was present as Cu^{2+} state (Fig. 3(d)). Overall, the XPS results show that Bi_2WO_6 bound successfully with CuS nanoparticles.

The optical properties of Bi_2WO_6/CuS were studied by UV-vis DRS. The spectrum of CuS had a gradually increasing absorption band at 250–750 nm (Fig. 4(a)), which may explain the greenness and blackness of the material. The absorption of Bi_2WO_6 was weak in the visible region, around 400 nm (Xu et al., 2019). However, compared with Bi_2WO_6, Bi_2WO_6/CuS had a wider visible-light response. Meanwhile, the absorption intensity of visible-light increased with the CuS mole ratio, which maybe due to the intrinsic absorption of CuS. The Kubelka-Munk equation was used to calculate the forbidden band width of the Bi_2WO_6/CuS heterojunction.

$$(\alpha h\nu)^2 = \mathrm{A}(h\nu - E_g), \tag{4}$$

where, α represents the absorption coefficient, h denotes Planck's constant, ν is the frequency, E_g is the band gap energy, and A is a constant that usually has a value of 1. The E_g values of Bi_2WO_6 and Bi_2WO_6/CuS-3 were 2.89 eV and 2.15 eV, respectively, as shown in Fig. 4(b).

To better understand the effect of the heterojunction coupling on the photocatalytic performance, the conduction band (CB) and valence band (VB) electric potentials for Bi_2WO_6 and Bi_2WO_6/CuS-3 were calculated using the following equations:

$$E_{CB} = X - E_C - E_g/2, \tag{5}$$

$$E_{VB} = E_{CB} - E_g, \tag{6}$$

where E_{CB} is the CB electric potential, E_{VB} is the VB electric potential, E_C is the energy of free electrons on the

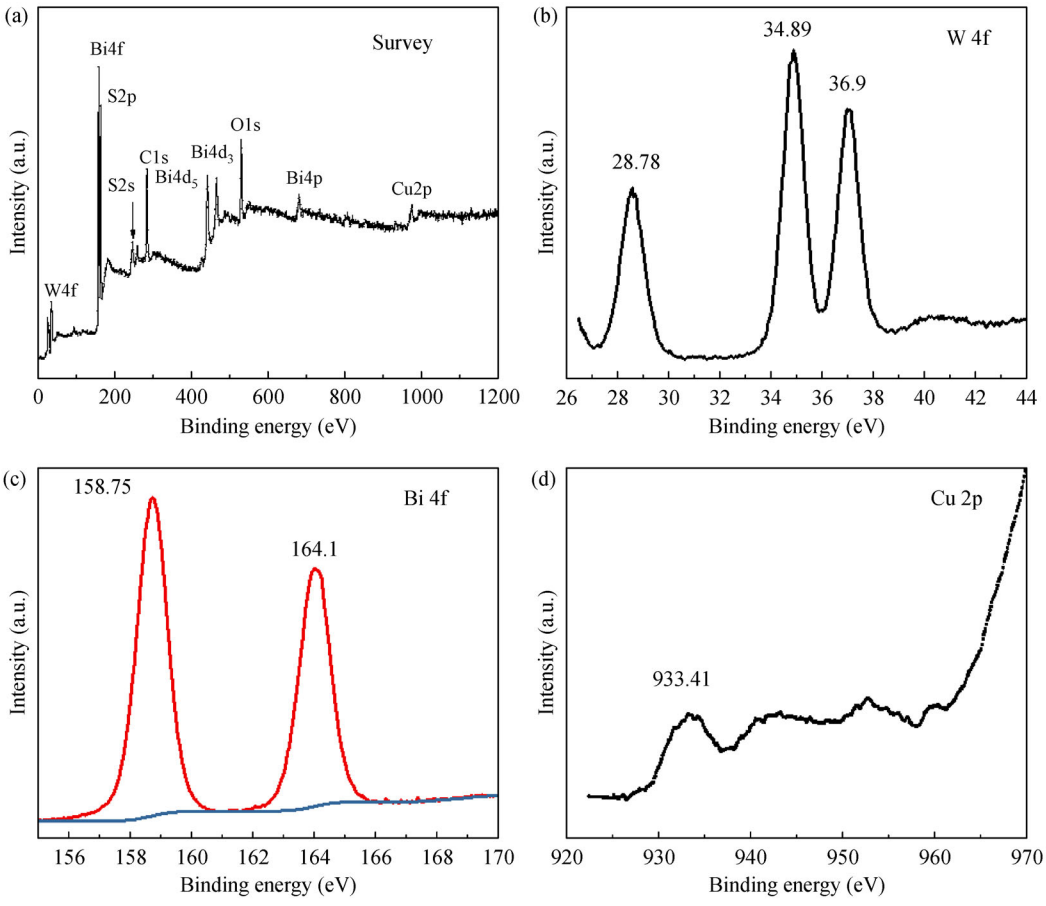

Fig. 3 XPS spectra of Bi_2WO_6/CuS-3: (a) survey spectra, (b) W 4f, (c) Bi 4f, and (d) Cu 2p.

hydrogen scale (about 4.5 eV), and X is the electronegativity of the semiconductor (Table S1). The VB potentials of Bi_2WO_6 and Bi_2WO_6/CuS-3 were +2.48 eV and +1.83 eV, respectively, and their CB potentials were 0.41 eV and −0.32 eV, respectively. These results were consistent with the Mott-Schottky measurements (Fig. S2). In conclusion, the Bi_2WO_6/CuS synthesized by the solvothermal reaction has a shorter band gap and improved the visible-light response.

The Bi_2WO_6/CuS photocatalytic performance was explored using EIS and PL spectra to examine the generation, separation, and migration of photoelectron-holes during photocatalytic cracking. The Nyquist diagram shows that a small arc radius results in a low charge separation resistance and faster transfer of photoexcited electrons (Liu et al., 2016). As shown in Fig. 4(c) and Fig. S3, Bi_2WO_6/CuS-3 had a smaller arc radius than the other Bi_2WO_6/CuS species. This suggests that the modification of CuS may accelerate the interfacial charge transfer and generate an instantaneous current, due to the formation of p-n heterojunctions.

The recombination of electrons and holes photoinduced by Bi_2WO_6/CuS was studied using PL spectroscopy. Lower PL emissions intensity indicates a lower recombination rate (Mao et al., 2018). The PL intensity of Bi_2WO_6/CuS decreased gradually with the increasing mole ratios of CuS (Fig. 4(d)), indicating that the photogenerated carrier separation efficiency increased with the mole ratio of CuS. This was mainly ascribed to the Bi_2WO_6/CuS forming p-n heterojunctions, shortening the band gap, and accelerating electron-hole separation. Meanwhile, doping S from CuS replaced oxygen in the lattice of Bi_2WO_6, forming lattice defects that inhibited electron-hole recombination.

3.2 Photocatalytic removal of RhB, TCH, and Cr(VI) in single solution

The photoactivity of the Bi_2WO_6/CuS samples was determined by their ability to degrade RhB under visible-light irradiation (Fig. 5(a)). The photodegradation efficiency in descending order was Bi_2WO_6/CuS-3>Bi_2WO_6/CuS-4>Bi_2WO_6/CuS-1>Bi_2WO_6/CuS-2>Bi_2WO_6>CuS>Dark. The best photocatalytic performance was by Bi_2WO_6/CuS-3, approximately 99.9% after the suspension was irradiated under visible-light for 60 min (Fig. S4), with the pseudo-first-order rate constant (K) reaching 0.0659 min^{-1} (Figs. 5(b) and S5(a)). This result illustrates that an appropriate and effective loading of CuS enhances

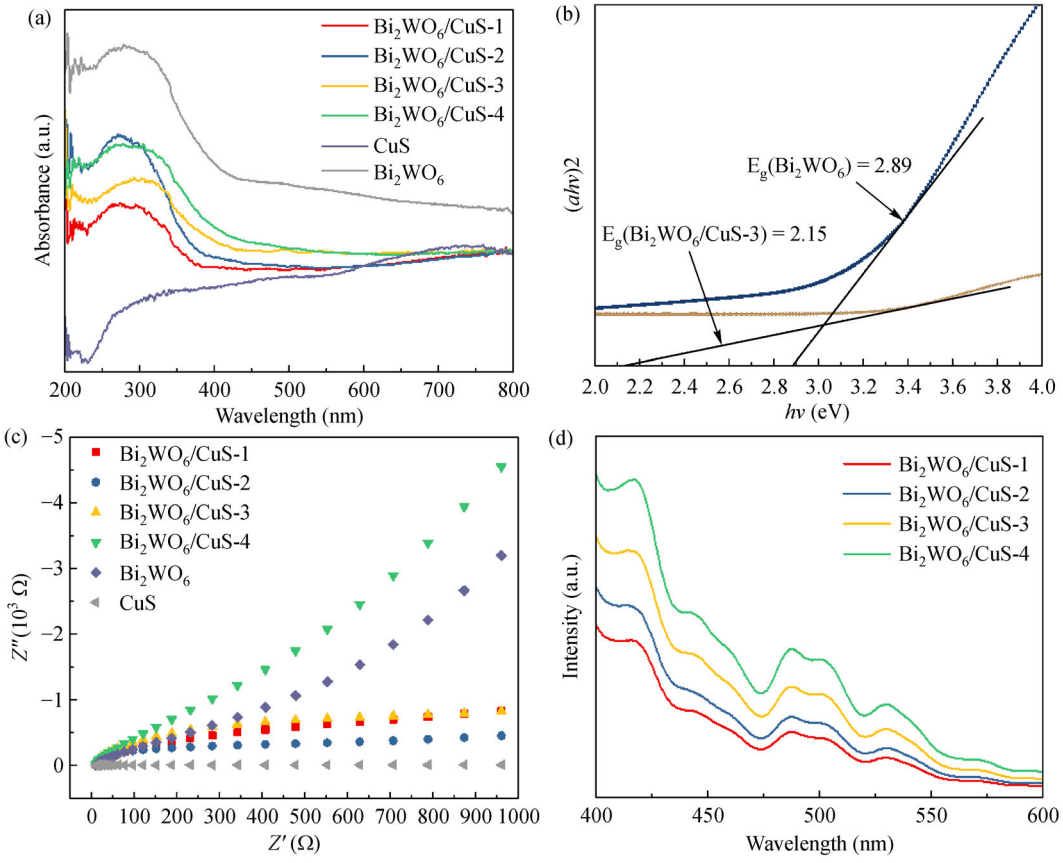

Fig. 4 Results of (a) UV-vis DRS, (b) band gaps, (c) EIS Nyquist, and (d) PL spectra of photocatalysts.

the photocatalytic activity. As time progressed, the absorption peak of RhB gradually weakened (Fig. 5(c)) and the color of the supernatant solutions faded (Fig. 5(d)). The maximum absorption peak of the mixed solution weakened significantly and exhibited slight hypsochromic shifts, which were caused by the stepwise formation of *N*-de-ethylated intermediates, such as *N*,*N*,*N*'-Triethyl-Rhodamine (TER), *N*-ethyl-*N*'-ethyl-Rhodamine (EER), *N*,*N*'-Diethyl-Rhodamine (DER), N-Ethyl-Rhodamine (ER), and rhodamine (R). Moreover, the degradation efficiency of RhB increased with the catalyst dosage because more electron-holes pairs and more active sites were produced (Fig. S6(a)). The initial concentration of RhB was varied from 2 to 50 mg/L while the other experimental parameters were kept constant (Fig. S6(b)). When the RhB concentration was 50 mg/L, the photodegradation efficiency was reduced by 15.38% for the following three reasons: 1) the transmittance of visible-light decreased as the RhB concentration increased, which led to a reduction in the visible light utilization efficiency of Bi_2WO_6/CuS; 2) the active surface sites of the Bi_2WO_6/CuS adsorbed the high concentration of RhB, which prevented photoexcited Bi_2WO_6/CuS from producing photoelectron-holes; 3) the RhB reaction by-products dominated competition for the active sites.

TCH was selected as a representative contaminant to determine the photocatalytic performance of Bi_2WO_6/CuS-3 because of its wide application in the pharmaceutical field. Bi_2WO_6/CuS-3 had good TCH degradation efficiency for initial contaminant concentrations in the range of 2 to 50 mg/L (Fig. 6). The adsorption efficiency of Bi_2WO_6/CuS-3 on TCH was almost zero in the dark and the degradation efficiency rapidly decreased from 99.0% to 16.4% with increasing TCH concentration. By contrast, the degradation efficiency of Bi_2WO_6/CuS-3 increased by 27.46% compared with Bi_2WO_6 (Fig. 6(a)), with the K value for 2 mg/L reaching 0.0174 min^{-1} (Figs. 6(b) and S5(b)). Photographs of the supernatant, which was sampled and centrifuged at corresponding time, also verified the degradation of TCH (Fig. 6(c)).

The reduction efficiency of Cr(VI) rapidly decreased from 98.8% to 34.6% as the concentration of Cr(VI) increased (Fig. 7(a)). Meanwhile, the reduction efficiency of Bi_2WO_6/CuS-3 increased by 15.2% compared to with Bi_2WO_6, with the K value for 5 mg/L reaching 0.0423 min^{-1} (Fig. 7(b)). It was clearly seen that the K value of 5 mg/L was 9.83 times larger than that for 35 mg/L and 17.63 times larger than that for Bi_2WO_6 (Fig. S5(c)). Table S2 compares the photocatalytic activity of Bi_2WO_6/CuS with that of other catalysts form the

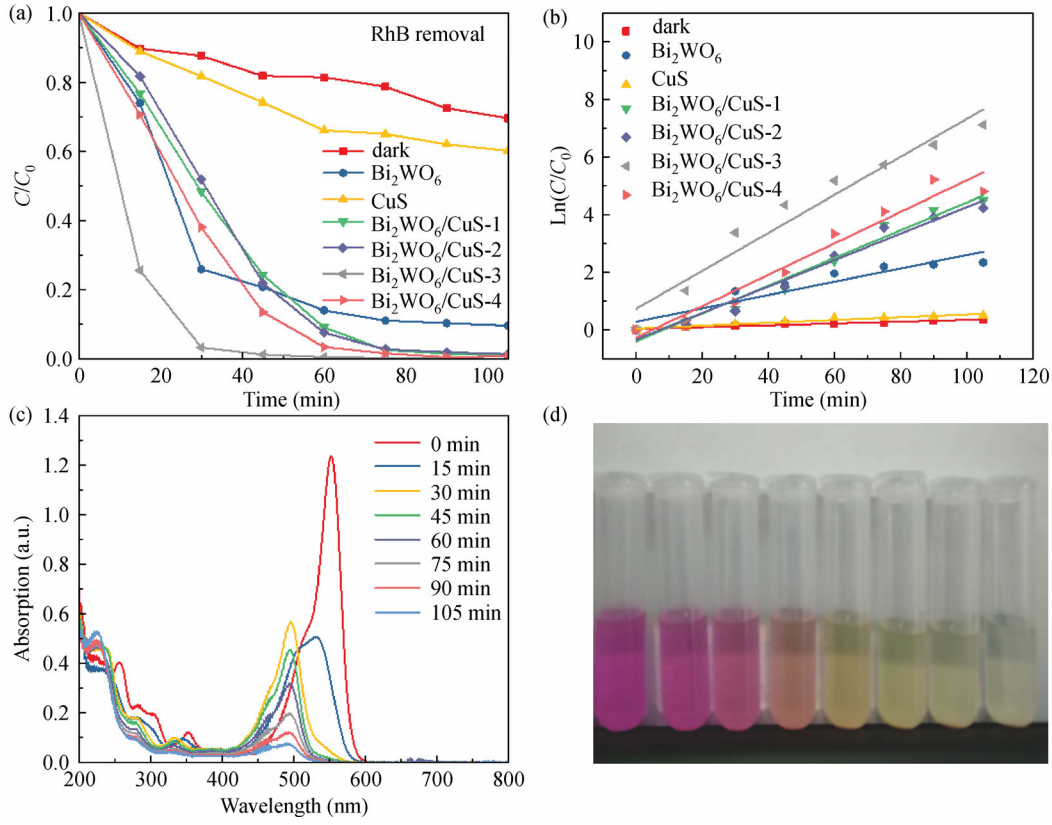

Fig. 5 (a) Photodegradation kinetics of RhB, (b) first-order kinetic model stimulation, (c) UV-visible spectra of RhB with Bi_2WO_6/CuS-3, and (d) photographs schematic. (Experimental conditions: 0.1 g photocatalyst, 100 mL solution, 10 mg/L RhB).

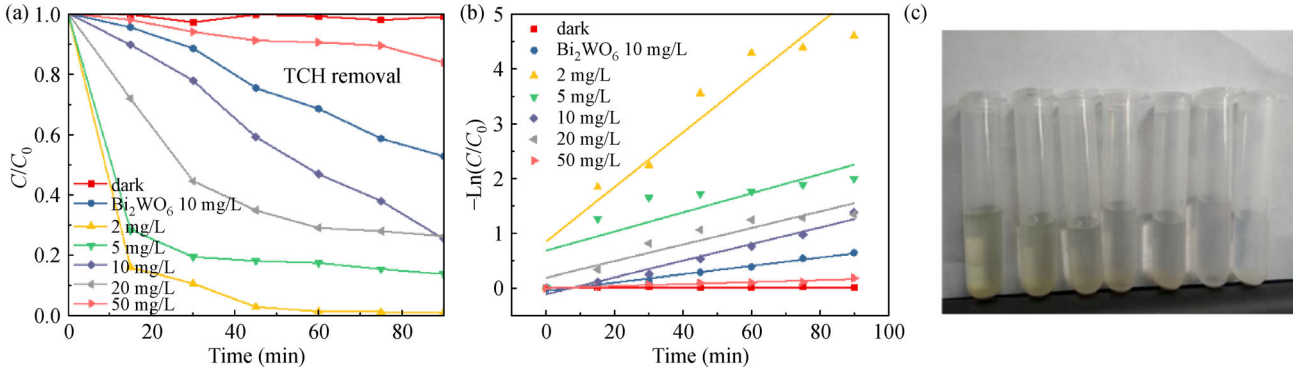

Fig. 6 (a) Photodegradation kinetics of TCH at different initial concentrations, (b) first-order kinetic model stimulation, and (c) photographs schematic. (Experimental conditions: 0.1 g photocatalyst, 100 mL solution, 2–50 mg/L TCH).

literature. Photographs of the supernatant, which was sampled by chromogenic reaction at corresponding times, also verified the removal of Cr(VI) (Fig. 7(c)).

3.3 Stability and reusability of photocatalysts

The stability and reusability of Bi_2WO_6/CuS-3 was analyzed by running four recycle experiments testing RhB degradation (Fig. S7). No significant reduction was observed in the photocatalytic performance of Bi_2WO_6/CuS-3 after the four consecutive recycle runs. Figure S8 shows that the flower-like hierarchical structure of Bi_2WO_6/CuS-3 was slightly damaged after the photocatalytic experiment, which could have been caused by the degradation of Bi_2WO_6/CuS-3 and the adsorption of contaminants on the surface. These was no significant difference in the main XRD characteristic peaks of Bi_2WO_6/CuS-3 between the initial and final recycle runs

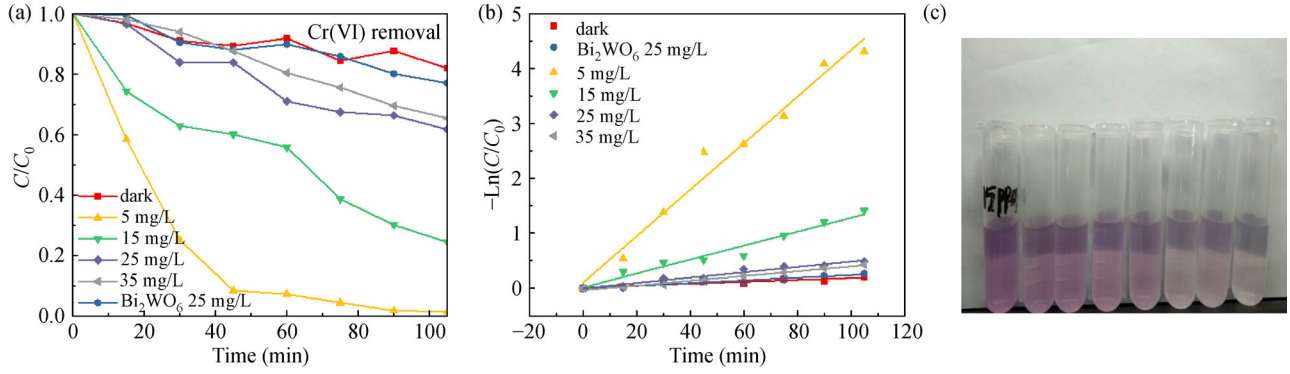

Fig. 7 (a) Photoreduction kinetics of Cr(VI) at different initial concentrations, (b) first-order kinetic model stimulation, and (c) Photographs schematic. (Experimental conditions: 0.1 g photocatalyst, 100 mL solution, 5–35 mg/L Cr(VI)).

(Fig. S9). This demonstrates that Bi_2WO_6/CuS-3 has excellent stability and recyclability for the photodegradation of contaminants, and consequently great potential for large-scale commercial production.

3.4 The photocatalytic performance of Bi_2WO_6/CuS in the mixed system

The photocatalytic performance of Bi_2WO_6/CuS was further explored in a mixed system made up of RhB (10 mg/L), TCH (10 mg/L) and Cr(VI) (15 mg/L). The blank experiment (no catalyst and dark conditions) showed that the removal efficiency of RhB, TCH, and Cr(VI) was basically zero (Fig. 8(a)), illustrating that no redox reactions involving the three contaminants occurred. In the presence of catalysts in dark conditions, the removal efficiencies of RhB, TCH, and Cr(VI) were 12.6%, 6.0%, and 22.3%, respectively (Fig. 8(b)). Although the degradation efficiency of RhB did not significantly decrease, the removal efficiencies of TCH and Cr(VI) increased remarkably in the RhB/TCH/Cr(VI) mixed system compared with their single pollution removal efficiencies. This was mainly attributed to the increased excitation number and enhanced separation efficiency of photogenerated carriers. Table S3 compares the photocatalytic performance of Bi_2WO_6/CuS for the simultaneous removal of RhB, TCH, and Cr(VI) with that of other catalysts from the literature.

Because the addition of Cr(VI) increased the photocatalytic removal efficiency by consuming electrons in the mixed system, experiments were carried out on the 100 mL mixture samples containing RhB (10 mg/L), TCH (10 mg/L), and Cr(VI) (5–35 mg/L) to explore the optimum Cr(VI) concentration. As shown in Figs. S10(a) and S10(b), the presence of low concentrations of Cr(VI) at first facilitated the photodegradation of RhB and TCH, but these degradation efficiencies slightly decreased with increased Cr(VI) concentration. The optimum degradation

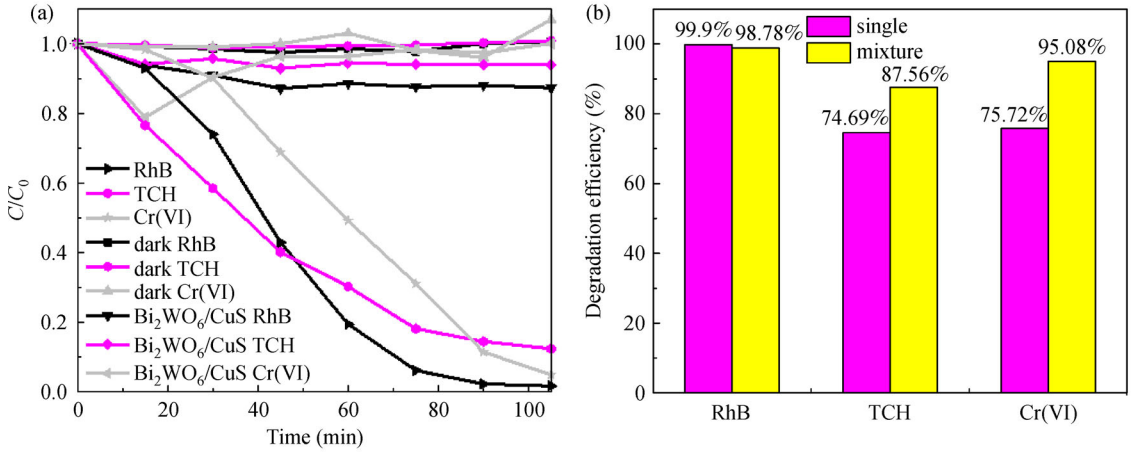

Fig. 8 (a) Results of simultaneous photocatalytic removal of RhB, TCH, and Cr(VI) in mixed systems and (b) comparison of photocatalytic removal efficiencies of RhB, TCH, and Cr(VI) in single and mixed systems. (Experimental conditions: 0.1 g Bi_2WO_6/CuS-3, 100 mL solution, 10 mg/L RhB, 10 mg/L TCH, and/or 15 mg/L Cr(VI)).

efficiencies of RhB and TCH were improved by 1.7% and 29.4%, respectively. This result demonstrates that the presence of appropriate concentrations of Cr(VI) in mixed solutions can accelerate the degradation of RhB and TCH. This is an excellent example of the simultaneous and efficient photocatalytic removal of organic pollutants and Cr(VI) from mixed wastewater and shows the potential of photocatalytic technology for the treatment of industrial mixed wastewater.

The effects of catalyst dosage on the removal of organic pollutants and Cr(VI) from the mixed solution were investigated (Fig. S11). The removal efficiencies of RhB (from 97.7% to 99.9%), TCH (from 76.8% to 98.7%) and Cr(VI) (from 76.9% to 99.9%) from the mixed solution were significantly improved by increasing the dose of catalyst because of the increased number of active sites on the Bi_2WO_6/CuS-3 surface and enhanced photogenerated electrons and holes.

In the mixed solution, pH has a strong impact on the oxidation potential, adsorption capacity, distribution of active sites on the catalyst surface, oxidation of organic pollutants, and reduction of Cr(VI). Table S4 shows that the initial pH was lower than the final pH in acidic conditions, but that the opposite was true in alkaline conditions, demonstrating that the process of photocatalytic reaction consumed hydrogen ions and hydroxide ions, The reduction of Cr(VI) consumed most of the H^+ (Liang et al., 2015). The degradation efficiencies of organic pollutants and Cr(VI) under acidic conditions were higher than under alkaline conditions (Fig. S12), which is ascribed to the increased oxidation of Cr(VI) in acidic conditions to promoting the efficient separation of electrons and holes. Usually, when the pH exceeds 6, Cr $(OH)_3$ is deposited on the Bi_2WO_6/CuS-3 surface, covering active sites and reducing the photocatalytic efficiency (Li et al., 2018a).

In natural environments, DOM, such as glucose, is ubiquitous. DOM contains some functional groups such as carboxyl and hydroxyl groups, that can indirectly and directly connect on the Bi_2WO_6/CuS-3 surface and form complexes with Cr(VI). Figure S13 shows the impact of glucose concentration on the photocatalytic treatent of the mixed solution. The photocatalytic performance improved with increasing glucose concentration. The optimal glucose concentration of 0.03 mol/L resulted in a remarkable improvement in the removal of RhB, TCH and Cr(VI) from 97.7%, 77.7%, and 76.9% to 98.1%, 87.2%, and 97.5%, respectively. The main reasons are as follows: 1) glucose contains an abundance of carboxyl and hydroxyl groups, which create an acidic environment for photocatalytic reactions (Zheng et al., 2014); 2) organic functional groups of glucose improve surface complexation to enhance the utilization rate of photogenerated electrons; 3) under visible-light irradiation, organic functional groups of glucose produces radicals that accelerate the removal of contaminants.

3.5 Possible photocatalytic mechanisms

Based on the above results, the probable photocatalytic mechanism by which Bi_2WO_6/CuS-3 degrades RhB, TCH, and Cr(VI) was proposed (Fig. 9). The photoexcitation under visible-light irradiation of Bi_2WO_6/CuS-3 generates electrons and holes. The photoelectrons jump into the CB, leaving the holes in the VB. Because of the p-n heterojunction construction and close contact with Cu–O bonds, the band gap of Bi_2WO_6/CuS-3 shortens to 2.15 eV from 2.89 eV (Fig. 4(b)). The CB potential of CuS is more negative than Bi_2WO_6, resulting in the transfer of excited electrons from CuS to the CB of Bi_2WO_6, while the resulting holes in the VB of Bi_2WO_6 are transported to that of CuS. This promotes the effective separation and migration of photogenerated charges. Because the CB potential of Bi_2WO_6 (+ 0.41 eV vs NHE) is more positive than the reduction potential (–0.046 eV vs NHE) of O_2/O^{2-} and the VB potential of CuS is more negative than that of $\cdot OH/H_2O$, the photoinduced electrons in the CB of Bi_2WO_6 can not be trapped to from O^{2-}, and holes are unable to oxidize H_2O to produce $\cdot OH$. Hence, the photogenerated electrons-holes can transfer to the surface of Bi_2WO_6/CuS to remove contaminants directly.

In addition, RhB can be excited to RhB* states under visible-light because of photosensitization (Fang et al., 2019), with the lower redox potential reaching –1.42 V vs. NHE (RhB*), making it much easier to oxidize (Fig. 9(a)) (He et al., 2014). Because the CB of Bi_2WO_6/CuS-3 is more positive than the redox potential of RhB^*/RhB^+, electrons from RhB* are transferred to the CB of Bi_2WO_6/CuS-3, converting RhB molecules to RhB^+, which promotes further oxidation of RhB by h^+. During the oxidation process, a series of N-de-ethylated intermediates are produced by photosensitization and eventually converted to CO_2 and H_2O. TCH is adsorbed on the surface of the Bi_2WO_6/CuS because of its large surface area and abundant micropores (Fig. 9(b)). TCH is oxidized directly by photogenerated holes and produces two intermediate products by demethylation (Zhu et al., 2019). These organic intermediates are eventually oxidized to CO_2, H_2O, and other species (Fig. 9(c)). Additionally, the electrons from the CB of Bi_2WO_6 can also directly reduce Cr(VI) to Cr(III) under ambient conditions (Yuan et al., 2019).

The possible removal mechanisms in the mixture solution are illustrated in Fig. 9(d) to more clearly show the simultaneous and efficient removal process. Organic pollutants and Cr(VI) serve as scavengers for each other and may consume photoinduced carriers concurrently, resulting in a synergy between the oxidation of organic pollutants and the reduction of Cr(VI). This synergy may significantly improve the migration of photogenerated electrons and holes and increase the utilization of charge carriers (Bai et al., 2018). Furthermore, the abundant organic functional groups of glucose (i.e., carboxyl and

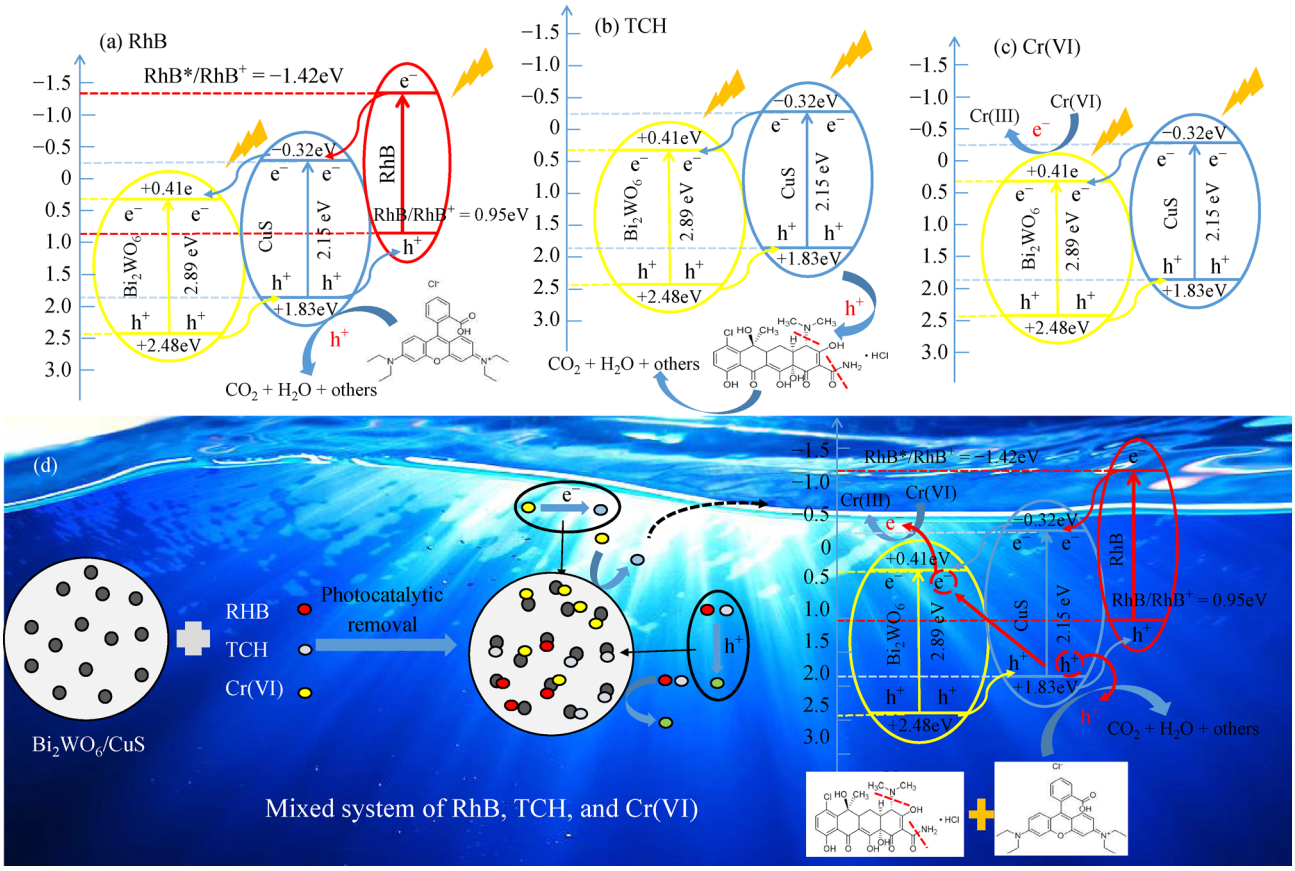

Fig. 9 Illustration of photocatalytic removal mechanisms of pure (a) RhB, (b) TCH, and (c) Cr(VI), and (d) mixed RhB, TCH, and Cr (VI) from wastewater by Bi_2WO_6/CuS-3 under visible-light irradiation.

hydroxyl) with Cr(VI) form complexes attached to the surface of Bi_2WO_6/CuS. The glucose likely serves as the hole scavenger and improves the efficiency of the transport/separation of photogenerated electrons and holes (Chong et al., 2014). In addition, glucose can be oxidized to produce radicals and hydrogen ions, that promote the degradation of RhB and TCH and create an acidic environment that increases the reduction of Cr(VI) to Cr(III) (Wang et al., 2019b).

4 Conclusions

Solid state Bi_2WO_6/CuS nanocomposites were successfully synthesized by a high-yield solvothermal route for loading CuS on the surface of Bi_2WO_6. The Bi_2WO_6/CuS showed outstanding photocatalytic performance for RhB, TCH, and Cr(VI) under visible-light irradiation, with optimum photocatalytic activity for RhB (10 mg/L, 99.9%), TCH (10 mg/L, 74.7%) and Cr(VI) (15 mg/L, 75.7%) as single contaminants. Subsequently, Bi_2WO_6/CuS-3 showed good removal efficiency of RhB (10 mg/L, 97.7%), TCH (10 mg/L, 87.6%) and Cr(VI) (15 mg/L, 95.1%) in mixed solution. The increased photocatalytic activity in the mixed solution is ascribed to increases in the number of photoinduced carriers and the migration efficiencies of photogenerated electrons and holes. The photocatalytic activity of Bi_2WO_6/CuS in mixed solution was only weakly pH-dependent in the pH range studied (pH = 2–6), suggesting that $Cr(OH)_3$ was the predominant species and competed for active sites on the catalyst surface to hinder the photocatalytic reaction in slightly alkaline conditions. Surface complexation of the carboxyl and hydroxy groups present in DOM with Cr(VI) accelerated the simultaneous and efficient removal of organic pollutants and Cr(VI). Overall, the performance of Bi_2WO_6/CuS in simultaneously and efficiently removing organic pollutants and Cr(VI) from mixed wastewater makes it a compelling candidate for industrial wastewater treatment.

Acknowledgements The present work was financially supported by the Major Science and Technology Program for Water Pollution Control and Treatment, National Water Grant (No. 2017ZX07202002); the National Natural Science Foundation of China (Grant No. 51979141); and the Key Research and Development Program of Guangdong Province (No. 2019B110205003).

Electronic Supplementary Material Supplementary material is available in the online version of this article at https://doi.org/10.1007/s11783-020-1344-8 and is accessible for authorized users.

References

Ahmadi M, Padervand M, Vosoughi M, Roosta Azad R (2017). Facile template-free synthesis of the CuO microflowers with enhanced photocatalytic properties. Materials Research Innovations, 21(7): 434–438

Ali A, Baheti V, Militky J (2019). Energy harvesting performance of silver electroplated fabrics. Materials Chemistry and Physics, 231: 33–40

Bai X, Du Y, Hu X, He Y, He C, Liu E, Fan J (2018). Synergy removal of Cr(VI) and organic pollutants over RP-MoS_2/rGO photocatalyst. Applied Catalysis B: Environmental, 239: 204–213

Bai Y, Zhao J, Feng S, Liang X, Wang C (2019). Light-driven thermocatalytic CO_2 reduction over surface-passivated beta-Mo_2C nanowires: Enhanced catalytic stability by light. Chemical Communications (Cambridge), 55(32): 4651–4654

Chen P, Chen L, Zeng Y, Ding F, Jiang X, Liu N, Au C T, Yin S F (2018). Three-dimension hierarchical heterostructure of $CdWO_4$ microrods decorated with Bi_2WO_6 nanoplates for high-selectivity photocatalytic benzene hydroxylation to phenol. Applied Catalysis B: Environmental, 234: 311–317

Chong R, Li J, Ma Y, Zhang B, Han H, Li C (2014). Selective conversion of aqueous glucose to value-added sugar aldose on TiO_2-based photocatalysts. Journal of Catalysis, 314: 101–108

Fang J, Zhang P, Chang H, Wang X (2018). Hydrothermal synthesis of nanostructured CuS for broadband efficient optical absorption and high-performance photo-thermal conversion. Solar Energy Materials and Solar Cells, 185: 456–463

Fang Z, Li Q, Su L, Chen J, Chou K C, Hou X (2019). Efficient synergy of photocatalysis and adsorption of hexavalent chromium and rhodamine B over Al_4SiC_4/rGO hybrid photocatalyst under visible-light irradiation. Applied Catalysis B: Environmental, 241: 548–560

Gao L, Du J, Ma T (2017). Cysteine-assisted synthesis of CuS-TiO_2 composites with enhanced photocatalytic activity. Ceramics International, 43(12): 9559–9563

Guo L, Zhang K, Han X, Zhao Q, Wang D, Fu F (2019). 2D In-plane CuS/Bi_2WO_6 p-n heterostructures with promoted visible-light-driven photo-Fenton degradation performance. Nanomaterials (Basel, Switzerland), 9(8): 1151

He J, Wang J, Chen Y, Zhang J, Duan D, Wang Y, Yan Z (2014). A dye-sensitized Pt@UiO-66(Zr) metal-organic framework for visible-light photocatalytic hydrogen production. Chemical Communications (Cambridge), 50(53): 7063–7066

Huang T, Li Y, Wu X, Lv K, Li Q, Li M, Du D, Ye H (2018). In-situ transformation of Bi_2WO_6 to highly photoreactive Bi_2WO_6 @Bi_2S_3 nanoplate via ion exchange. Chinese Journal of Catalysis, 39(4): 718–727

Li F, Wang L, Han X, Cao Y, He P, Li H (2017). Selective hydrogenation of ethylene carbonate to methanol and ethylene glycol over Cu/SiO_2 catalysts prepared by ammonia evaporation method. International Journal of Hydrogen Energy, 42(4): 2144–2156

Li J, Peng T, Zhang Y, Zhou C, Zhu A (2018a). Polyaniline modified SnO_2 nanoparticles for efficient photocatalytic reduction of aqueous Cr(VI) under visible light. Separation and Purification Technology, 201: 120–129

Li X, Xie J, Jiang C, Yu J, Zhang P (2018b). Review on design and evaluation of environmental photocatalysts. Frontiers of Environmental Science & Engineering, 12(5): 14

Liang R, Shen L, Jing F, Wu W, Qin N, Lin R, Wu L (2015). NH_2-mediated indium metal–organic framework as a novel visible-light-driven photocatalyst for reduction of the aqueous Cr(VI). Applied Catalysis B: Environmental, 162: 245–251

Liu L, Qi Y, Lu J, Lin S, An W, Liang Y, Cui W (2016). A stable Ag_3PO_4@g-C_3N_4 hybrid core@shell composite with enhanced visible light photocatalytic degradation. Applied Catalysis B: Environmental, 183: 133–141

Loy A C M, Quitain A T, Lam M K, Yusup S, Sasaki M, Kida T (2019). Development of high microwave-absorptive bifunctional graphene oxide-based catalyst for biodiesel production. Energy Conversion and Management, 180: 1013–1025

Mao W, Wang T, Wang H, Zou S, Liu S (2018). Novel Bi_2WO_6 loaded g-C_3N_4 composites with enhanced photocatalytic degradation of dye and pharmaceutical wastewater under visible light irradiation. Journal of Materials Science Materials in Electronics, 29(17): 15174–15182

Padervand M, Jalilian E (2019). $Bi_{24}Br_{10}$+ xAg$x$$O_{31}$ nanostructure, a new reusable photocatalyst for efficient removal of Acid Blue 92 from model wastewaters under visible light. Progress in Reaction Kinetics and Mechanism, 44(3): 257–266

Sharma V K, Yu X, Mcdonald T J, Jinadatha C, Dionysiou D D, Feng M (2019). Elimination of antibiotic resistance genes and control of horizontal transfer risk by UV-based treatment of drinking water: A mini review. Frontiers of Environmental Science & Engineering, 13 (3): 37

Wang L, Bahnemann D W, Bian L, Dong G, Zhao J, Wang C (2019a). Two‐dimensional layered zinc silicate nanosheets with excellent photocatalytic performance for organic pollutant degradation and CO_2 conversion. Angewandte Chemie International Edition, 58(24): 8103–8108

Wang L, Zhu W, Lu W, Shi L, Wang R, Pang R, Cao Y, Wang F, Xu X (2019b). One-step electrodeposition of AuNi nanodendrite arrays as photoelectrochemical biosensors for glucose and hydrogen peroxide detection. Biosensors & Bioelectronics, 142: 111577

Wang X, Feng X, Shang J (2018). Efficient photoelectrochemical oxidation of rhodamine B on metal electrodes without photocatalyst or supporting electrolyte. Frontiers of Environmental Science & Engineering, 12(6): 11

Xu F, Xu C, Chen H, Wu D, Gao Z, Ma X, Zhang Q, Jiang K (2019). The synthesis of Bi_2S_3/2D-Bi_2WO_6 composite materials with enhanced photocatalytic activities. Journal of Alloys and Compounds, 780: 634–642

Yuan R, Yue C, Qiu J, Liu F, Li A (2019). Highly efficient sunlight-driven reduction of Cr(VI) by TiO_2@NH_2-MIL-88B(Fe) heterostructures under neutral conditions. Applied Catalysis B: Environmental, 251: 229–239

Zargazi M, Entezari M H (2019). Anodic electrophoretic deposition of Bi_2WO_6 thin film: high photocatalytic activity for degradation of a binary mixture. Applied Catalysis B: Environmental, 242: 507–517

Zheng Z, Tachikawa T, Majima T (2014). Single-particle study of Pt-modified Au nanorods for plasmon-enhanced hydrogen generation in visible to near-infrared region. Journal of the American Chemical Society, 136(19): 6870–6873

Zhou H, Wen Z, Liu J, Ke J, Duan X, Wang S (2019). Z-scheme plasmonic Ag decorated WO_3/Bi_2WO_6 hybrids for enhanced photocatalytic abatement of chlorinated-VOCs under solar light irradiation. Applied Catalysis B: Environmental, 242: 76–84

Zhu Q, Sun Y, Na F, Wei J, Xu S, Li Y, Guo F (2019). Fabrication of CdS/titanium-oxo-cluster nanocomposites based on a Ti_{32} framework with enhanced photocatalytic activity for tetracycline hydrochloride degradation under visible light. Applied Catalysis B: Environmental, 254: 541–550

Zhu Y, Wang Y, Ling Q, Zhu Y (2017). Enhancement of full-spectrum photocatalytic activity over $BiPO_4$/Bi_2WO_6 composites. Applied Catalysis B: Environmental, 200: 222–229